



Trans. Nonferrous Met. Soc. China 32(2022) 1852-1865

Transactions of Nonferrous Metals Society of China

www.tnmsc.cn



Characteristics and formation mechanisms of defect bands in vacuum-assisted high-pressure die casting AE44 alloy

Ying-ying HOU¹, Meng-wu WU¹, Bing-hui TIAN¹, Xiao-bo LI², Shou-mei XIONG²

1. Hubei Key Laboratory of Advanced Technology for Automotive Components, Wuhan University of Technology, Wuhan 430070, China;

2. School of Materials Science and Engineering, Tsinghua University, Beijing 100084, China

Received 15 May 2021; accepted 10 December 2021

Abstract: The microstructure in vacuum-assisted high-pressure die casting (HPDC) Mg-4Al-4RE (AE44) alloy was studied. Special attention was paid to the characteristics of defect bands and their formation mechanisms. Since double defect bands are commonly observed, the cross section of die cast samples is divided into five parts with different grain morphologies and size distributions. The inner defect band is much wider than the outer one. Both the defect bands are solute segregation bands, resulting in a higher area fraction of Al₁₁RE₃ phase than that in the adjacent regions. No obvious aggregation of porosities is observed in the defect bands of AE44 alloy. This may be due to a narrow solidification temperature range of AE44 alloy and a large amount of latent heat released during the precipitation of intermetallic phases. The formation of the defect bands is related to the shear stress acting upon the partially solidified alloy, which can lead to collapse of the grain network. However, the generation mechanisms of shear stress in the outer and inner defect bands are quite different.

Key words: high-pressure die casting; magnesium alloy; AE44; microstructure; defect band

1 Introduction

Under the global trend of energy conservation and environmental protection, magnesium alloy, as the lightest structural material, has already become a strong candidate to replace traditional metal materials to achieve mass reduction [1–4]. However, the large-scale application of magnesium alloy still faces several challenges. Taking the commonly used commercial Mg–Al alloys, such as Mg–6Al–0.3Mn (AM60) and Mg–9Al–0.7Zn–0.2Mn (AZ91) for example, though these alloys exhibit excellent castability and a good combination of strength and ductility at room temperature, they do not have adequate high-temperature strength and creep resistance above 400 K [5–7]. Therefore, their use was restricted to room-temperature applications.

Addition of rare earth elements (RE) such as Ce and La is known to improve high-temperature strength and creep resistance of Mg–Al base alloys [8,9]. In this respect, the representative magnesium alloys include Mg–4Al–2RE (AE42) and later AE44 [10]. For cast Mg-alloy products, the high-pressure die casting (HPDC) process is the preferred and dominant manufacturing process with the advantages of high efficiency, considerable economic benefit and high precision of the product size [11–13]. In particular, for AE serials alloys, the high cooling rate during the HPDC process can suppress the formation of coarse Al–RE intermetallic phases, which is beneficial to the mechanical properties of castings [14].

On the other hand, the HPDC process has its deficiencies. Casting defects including gas pores, externally solidified crystals (ESCs) and defect

bands often exist in the final microstructure of die castings, while these defects rarely appear in components produced by conventional casting processes [15–17]. Extensive studies have been conducted on formation mechanisms, morphology and distribution of gas pores and ESCs in the microstructure of die castings, and their effects on the mechanical properties of components [18–21]. Meanwhile, modifications have been made to the HPDC process with the purpose of reducing gas pores and ESCs [22–24].

As for the defect bands, they normally follow the outer contour of castings and contain positive macrosegregation and porosities [25]. With an average thickness of several grains, they are detrimental to the mechanical performance of die cast components [26]. Existing studies are mainly focused on the characterization of defect bands with varied casting conditions and their formation mechanisms. GOURLAY and DAHLE [27] pointed out that the origin of defect bands was related to the rheological and solidification behaviors of the partially solidified alloy and the filling pattern of castings with associated shearing of the mushy zone. CAO and WESSEN [28] found that the intensification pressure had the strongest influence on the appearance of defect bands by investigating the microstructure in die cast AM50 components, and defect bands were more likely to appear in thick or heavy components. GOURLAY et al [29] pointed out that defect bands could be formed both near to and relatively far from any surface layer of different microstructures in HPDC AZ91 and AM60 alloys. Meanwhile, the ESCs were not necessary for defect band formation. OTARAWANNA et al [30] reported that the defect band thickness was in the range of 7-18 mean grains wide, and multiple bands were observed in the cross section of die cast AM50 sample. LI et al [31] investigated different melt flow patterns in HPDC AZ91D alloy, and found that the crystals in the contour of the melt flow would rotate and fragment under the flush of melt flow, leading to a large gap among crystals and then the formation of defect bands. HUANG et al [32] found that multiple dilatant bands tended to appear in the thick section of castings, and the skin related band was likely to form near the concave corner of the cross section. Through literature review, though there have been some research works reported on the characterization of defect bands in microstructure of traditional Mg-Al alloys, very few studies have been performed on the characteristics of microstructure and defect bands in die cast AE serials alloys. Furthermore, the formation mechanisms of defect bands in HPDC magnesium alloys are not yet very clear, especially the appearance of multiple defect bands in the cross section of die castings.

In this study, a specific casting was produced by vacuum-assisted HPDC process with AE44 magnesium alloy. Microstructure characterization of the component was conducted by using optical microscope (OM), scanning electron microscope (SEM), energy dispersive spectrometer (EDS), X-ray diffraction (XRD), electron back-scattered diffraction (EBSD) and transmission electron microscope (TEM). Qualitative and quantitative analysis was carried out on the morphology and distribution of defect bands, as well as the correlation between defect bands and porosities or ESCs, based on which the formation mechanisms of defect bands were discussed.

2 Experimental

During the experiment, a specific casting (Fig. 1) was produced by a TOYO BD-350V5 cold chamber die casting machine with a vacuum system assisted. Commercial AE44 magnesium alloy was used as the experimental material. According to the analysis of inductively coupled plasma (ICP), its composition is listed in Table 1. With the rare earth elements Ce and La as the main alloying elements

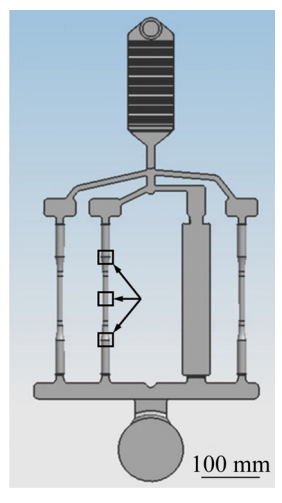


Fig. 1 Configuration of specific casting including three tensile test bars and one plate sample (All the specimens were extracted from the rectangular areas)

Table 1 Chemical composition of AE44 magnesium alloy (wt.%)

| Al | Ce | La | Mn | Li | Ca | Fe | Zn | Mg |
|------|------|------|------|------|------|------|------|------|
| 4.14 | 2.81 | 1.16 | 0.18 | 0.12 | 0.13 | 0.08 | 0.01 | Bal. |

besides Al, the liquidus and solidus temperatures of the alloy are 620 and 540 °C, respectively. Key process parameters adopted in the die cast experiment are listed in Table 2. During the slow shot stage of the HPDC process, an optimization was made for the slow shot speed. The plunger firstly moved in a constant speed of 0.3 m/s for 120 mm and then decelerated to 0.2 m/s for another 150 mm, after which the speed was switched to 2.75 m/s and the process stepped into the fast shot stage. Intensification casting pressure was applied when the plunger moved to 285 mm and maintained until the casting solidified.

Table 2 Key parameters used during HPDC process

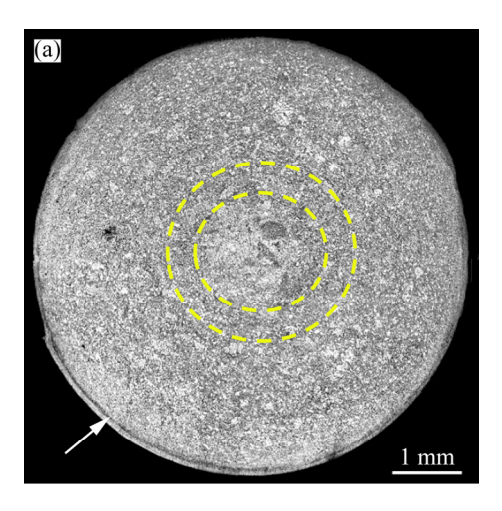
| Pouring | Initial mold | Slow shot | Fast shot | Casting |
|--------------|--------------|--------------------------------------|--------------------|-----------|
| temperature/ | temperature/ | speed/ | speed/ | pressure/ |
| °C | °C | $(\mathbf{m} \cdot \mathbf{s}^{-1})$ | $(m \cdot s^{-1})$ | MPa |
| 700 | 180 | 0.3, 0.2 | 2.75 | 13.7 |

With a gauge diameter of 6.4 mm, the middle tensile test bar was cut. All the specimens were extracted from the rectangular areas, as shown in Fig. 1. The middle and transition segments of the bar were chosen for microstructure characterization. A ZEISS scope A1 OM, a JSM-IT300 SEM and a FEI Talos F200X TEM were used for metallography observation. XRD was carried out on an Empyrean diffractometer using Cu K_{α} radiation in the range from 10° to 90° with a scanning speed of 6 (°)/min and a step of 0.02°. The testing data were then imported into Jade for further analysis. The grain orientation information of the specimens was calibrated by EBSD experiments performed with a ZEISS MERLIN Compact SEM with HKL Channel 5 system. Image Pro Plus 6.0 software was employed to perform a quantitative analysis of the microstructural features.

3 Results and discussion

3.1 Microstructure of cross section

Figure 2(a) shows the overall morphology of the microstructure of AE44 alloy at the cylindrical cross section of the middle tensile test bar. Two



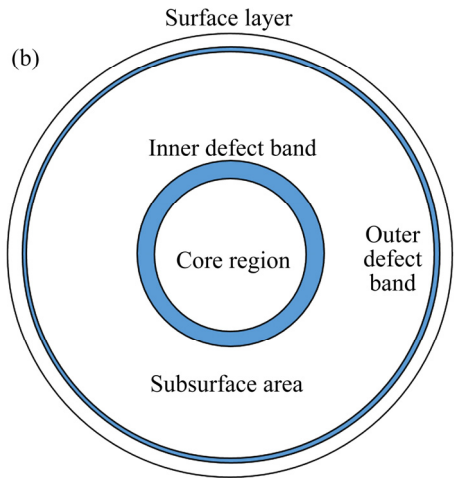


Fig. 2 Cylindrical cross section showing double defect bands: (a) OM image of cross section; (b) Illustration of division of cross section

ring-shape black bands appear in the OM image following the outer contour of the casting: one is located near the center and the other very close to the surface of the casting. Referring to previous studies, these bands are undoubtedly the so-called defect bands. Since double defect bands are commonly observed, the cross section can be divided into five parts, sequentially the surface layer, outer defect band, subsurface area, inner defect band and core region, as illustrated in Fig. 2(b). In-depth microstructure characterization of these parts was conducted. Figure 3 shows the OM images of different parts of the cross section. It can be found that there are extreme differences between these parts related to the grain morphology. Coarse and well-developed dendrites, namely externally solidified crystals (ESCs) are observed to mainly gather in the core region, as shown in Fig. 3(a), while a large number of spherical or

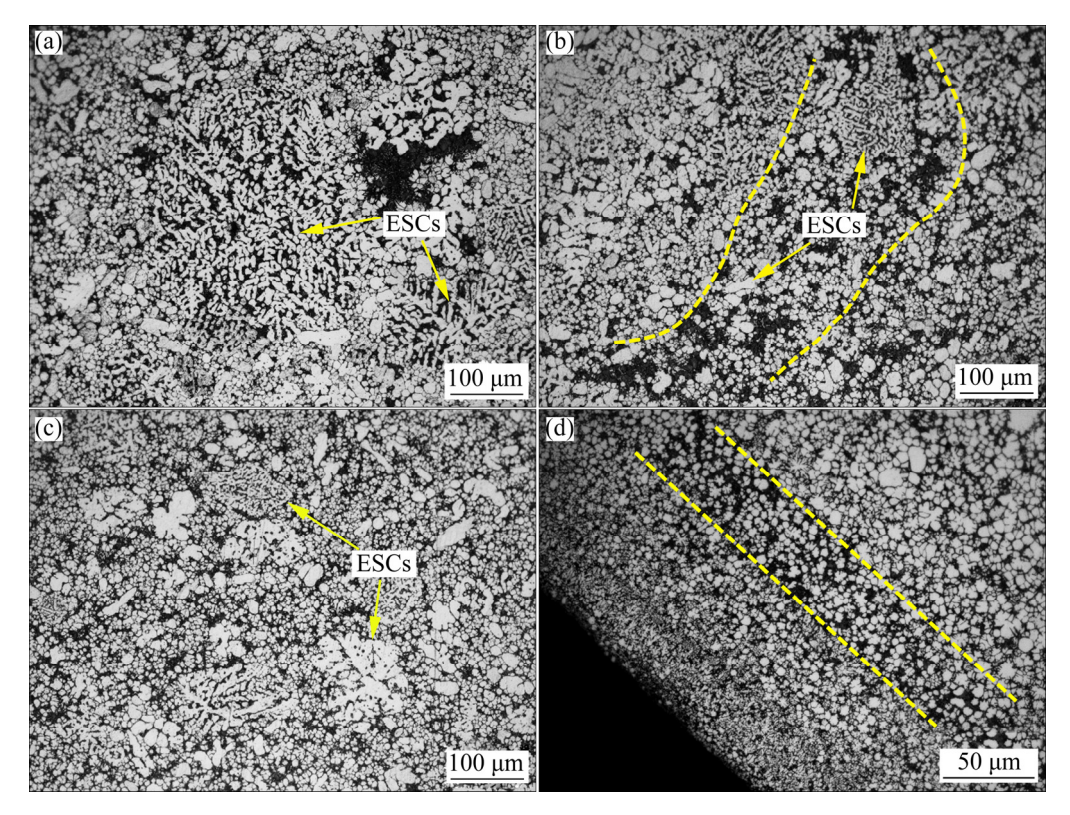


Fig. 3 OM images showing microstructure of different parts of cross section: (a) Core region; (b) Inner defect band; (c) Subsurface area; (d) Outer defect band and surface layer (The areas between the yellow dotted lines indicate the defect bands)

fragmented ESCs are scattered in the inner defect band and subsurface area (Figs. 3(b, c)). However, few or no ESCs appear in the outer defect band and surface layer, as illustrated in Fig. 3(d). LAUKLI et al [33] gave a reasonable explanation for this phenomenon. At the fast shot stage of the HPDC process, a mixture of liquid and ESCs which nucleate in the melt in the shot sleeve is injected into the die cavity. The floating ESCs migrate to the central region of the die cavity due to the force of the flowing melt. Meanwhile, some ESCs might encounter impact of the melt or remelt during the fast shot stage, resulting in a spherical or fragmented shape finally. Since a vacuum system was employed during the HPDC process in this experiment, the number of gas pores is significantly reduced in the microstructure of the casting. Large porosities, in the form of shrinkage are commonly observed in the core region, such as the dark island-shape one in the OM image, as shown in Fig. 3(a). However, as for the inner and outer defect bands, further investigations are required to confirm whether the dark areas represent porosities or not (Figs. 3(b, d)).

Figure 4 shows the grain orientation maps of different parts of the cross section obtained by EBSD. Based on a criterion that the orientation difference is less than 15° within the same grain, distinction of different grains and further statistics of the grain size in the microstructure of the cross section can be achieved. It can be seen from Figs. 4(a-c) that the microstructure comprises a mixture of coarse ESCs and fine grains. Arranging from high to low with respect to the area fraction of the ESCs, they are the core region, inner defect band and subsurface area in turn. The size of the basal fine grains is $5-30 \,\mu m$, while the equivalent grain size of the coarse ESCs is up to 100 µm. For the outer defect band and surface layer, uniform and fine grains are observed and a considerable number of grains have a grain size smaller than 5 μm (Figs. 4(d, e)).

By further comparing the characteristics of the two defect bands shown in Figs. 3(b, d), they are similar in overall appearance. A clear boundary can be observed between each defect band and the adjacent region. Meanwhile, both of them consist of sparse α -Mg grains and porosities or second phase

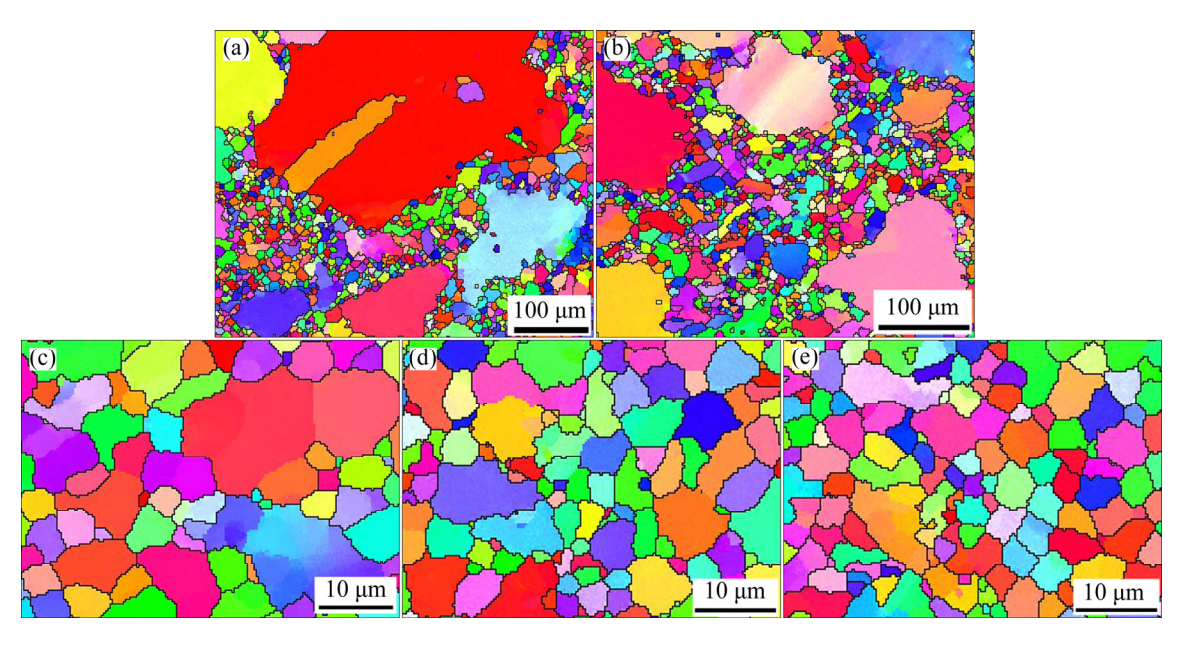


Fig. 4 Grain orientation maps of different parts of cross section obtained by EBSD: (a) Core region; (b) Inner defect band; (c) Subsurface area; (d) Outer defect band; (e) Surface layer

filled among the grains. The differences between the two defect bands are mainly concentrated in the width and internal grain morphology and size, as summarized in Table 3. With an irregular ring-shape morphology, the maximum width of the inner defect band is $321.2 \, \mu m$, and the minimum width is $95.2 \, \mu m$. With average width of $31.7 \, \mu m$, the outer defect band is much narrower than the inner one.

Table 3 Characteristics of defect bands

| Defect band | Minimum width/μm | | Average width/μm | Internal grains |
|----------------|---------------------|-------|---------------------|-----------------------------------|
| Inner | 95.2 | 321.2 | 191.3 | Coarse ESCs and fine grains |
| Outer | 19.4 | 45.2 | 31.7 | Fine grains |

Figure 5 indicates the average thickness proportions of the five parts of the cross section. It can be seen that the subsurface area makes up most of the cross section, followed by the core region, inner defect band, surface layer and outer defect band in turn. With the two defect bands separated by the subsurface area, they are far away from each other. This may be used to explain the difference in microstructure characteristics between the two defect bands, which also implies that the formation mechanism of the outer defect band may be quite different from the inner one. It is noteworthy that

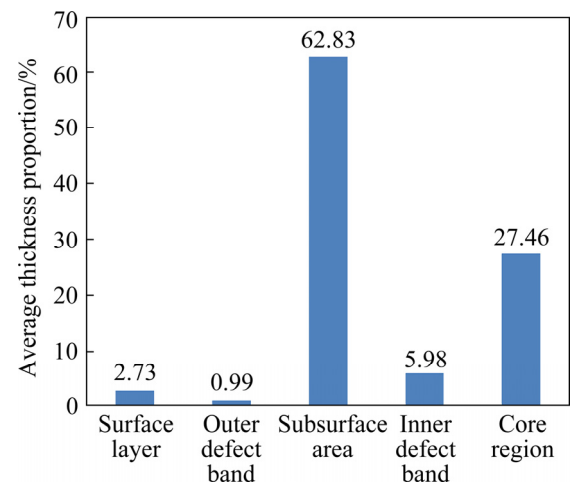


Fig. 5 Average thickness proportions of five parts of cross section

the thickness proportions of the two defect bands, especially the inner defect band, are large enough to affect the mechanical properties of the casting.

3.2 Phase morphology and distribution

Based on the composition of the AE44 magnesium alloy listed in Table 1, Al is the main alloying element, followed by the rare earth elements, Ce and La. Figure 6 shows the XRD pattern of the HPDC AE44 magnesium alloy, illustrating that the alloy mainly consists of α -Mg, Al₁₁RE₃ and Al₂RE phases. A conclusion can be made that the element Al preferentially reacts with

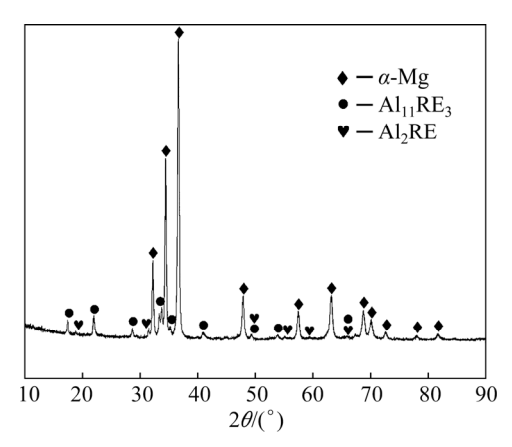


Fig. 6 XRD pattern of HPDC AE44 magnesium alloy

RE rather than Mg. Therefore, the commonly observed second phase in Mg–Al serials alloys, $Mg_{17}Al_{12}$, would not appear in the AE44 magnesium alloy. According to Table 1, the HPDC AE44 magnesium alloy may also contain other intermetallic phases, such as Al–RE–Mn phase. However, the amount of them is not sufficient enough to be detected by XRD in the present work.

To investigate the phase morphology and distribution in HPDC AE44 magnesium alloy, microstructure characterization was further conducted by SEM, TEM and EDS. Figure 7 illustrates the SEM images of the five parts of the cross section. There are two types of intermetallic phases, one with a lamellar-like morphology in light grey color and the other with a particulate shape in bright white color. Meanwhile, it can be seen that the lamellar-like phase is the dominant intermetallic phase and widely distributed between grain boundaries, while the particulate phase is scattered both within the grains and between grain boundaries.

According to the analysis of the selected area electron diffraction (SAED) patterns and EDS spectra shown in Fig. 8, identification of the two types of intermetallic phases is achieved. The particulate phase is identified to be Al₂RE with a diamond cubic structure whereas the lamellar-like one is Al₁₁RE₃ with a body-centered orthorhombic structure. It is worth mentioning that since the content of Ce is much higher than that of La in AE44 alloy, Ce is more easily to be detected by EDS, while La does not appear in the EDS spectra, as illustrated in Figs. 8(d, e).

By comparing the microstructure of different parts of the cross section as shown in Fig. 7, a

similar conclusion can also be drawn, i.e., the formation of ESCs and defect bands both lead to an inhomogeneous microstructure of the HPDC AE44 magnesium alloy. The microstructure consists of a mixture of coarse ESCs and fine grains in the core region, inner defect band and subsurface area. In this case, the Al₁₁RE₃ phase agglomerates among large grains and also dendrite branches, resulting in the formation of clusters of Al₁₁RE₃ phase with a long-lamellar shape. Due to a microstructure comprising uniform and fine grains, the Al₁₁RE₃ phase in the outer defect band and surface layer is dispersed and reveals a short-lamellar shaped morphology. It can be confirmed apparently from Fig. 7 that most of the dark areas in the OM images shown in Fig. 3, especially in the defect bands shown in Figs. 3(b, d), represent intermetallic phases, but not porosities. In other words, there are obvious differences between the five parts of the cross section related to the content of the intermetallic phases, particularly Al₁₁RE₃. Table 4 gives the statistical results of the area fraction of Al₁₁RE₃ in different parts of the cross section. It can be found that the content of Al₁₁RE₃ in both of the defect bands is higher than that of the adjacent regions. Five parts of the cross section with the content of Al₁₁RE₃ from high to low are the inner defect band, outer defect band, subsurface area, surface layer and core region. Consequently, both the two defect bands are bands with positive macrosegregation.

3.3 Comparison of defect bands in HPDC AE44 and AZ91D alloys

Unlike the previously reported defect bands in HPDC AZ91D alloy both with and without a vacuum system assisted [34,35], no obvious aggregation of porosities is observed in the defect bands of HPDC AE44 alloy in the present work. Except for the difference in process parameters of the HPDC process, the reason for this may be mainly attributed to the disparity between the solidification characteristics of the two alloys. thermodynamic calculations of phase transformation during equilibrium solidification of the two alloys were conducted by using the JMatPro 9.0 software and the results are illustrated in Fig. 9.

In AE44 alloy, nucleation and growth of α -Mg occur firstly in the early stage of solidification

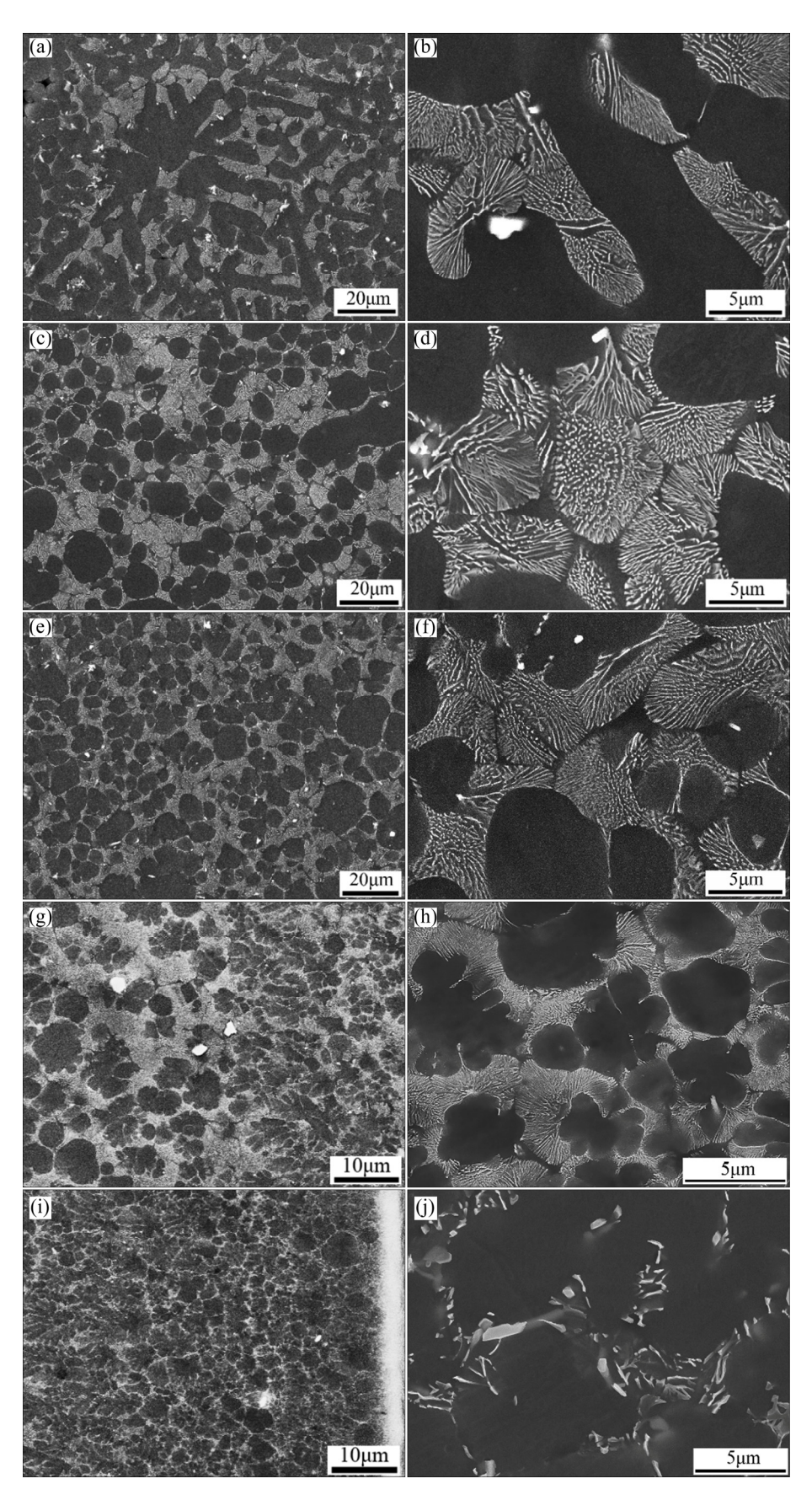


Fig. 7 SEM images showing microstructure of different parts of cross section: (a, b) Core region; (c, d) Inner defect band; (e, f) Subsurface area; (g, h) Outer defect band; (i, j) Surface layer

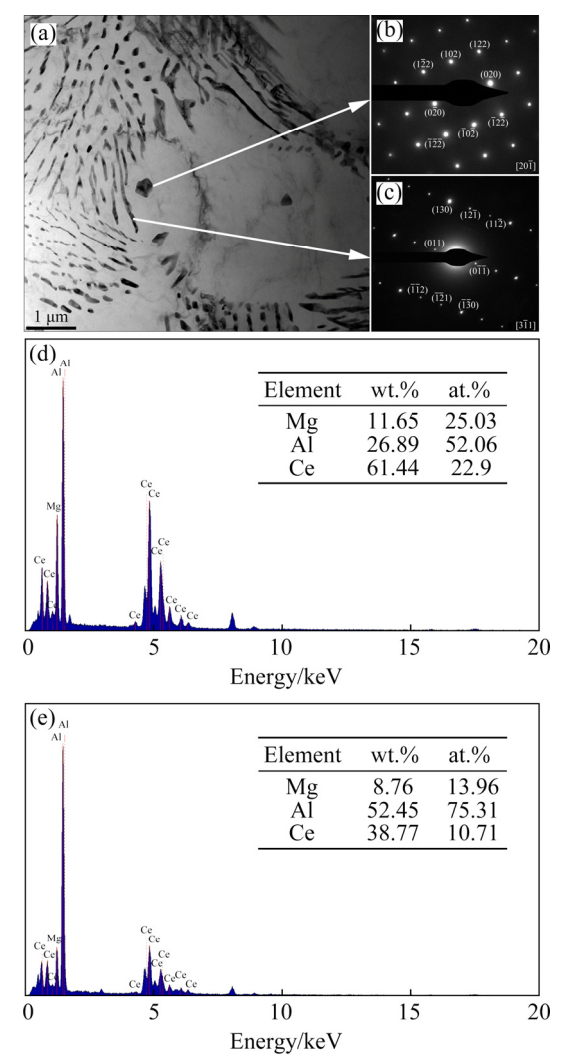


Fig. 8 Identification of intermetallic phases: (a) Brightfield TEM image of HPDC AE44 alloy; (b, c) SAED patterns of particulate-shaped phase and lamellar-like phase; (d, e) EDS spectra of particulate-shaped phase and lamellar-like phase

Table 4 Area fraction of Al₁₁RE₃ phase in different parts of cross section

| Core | Inner defect | Subsurface | Outer | Surface |
|--------|--------------|------------|-------------|---------|
| region | band | area | defect band | layer |
| 8.6% | 17.1% | 12.3% | 16.0% | 11.0% |

when the temperature of the melt goes below the liquidus temperature (620 °C). With the melt temperature dropping to 600 °C, the solid fraction of the melt is about 50%. As the solidification proceeds, Al₂RE, Al₃RE and Al₁₁RE₃ phases precipitate successively in the remaining solute-enriched melt. During this period, a considerable part of Al₂RE phase transforms into Al₃RE phase due to the supply of Al with the continuous nucleation and growth of α -Mg.

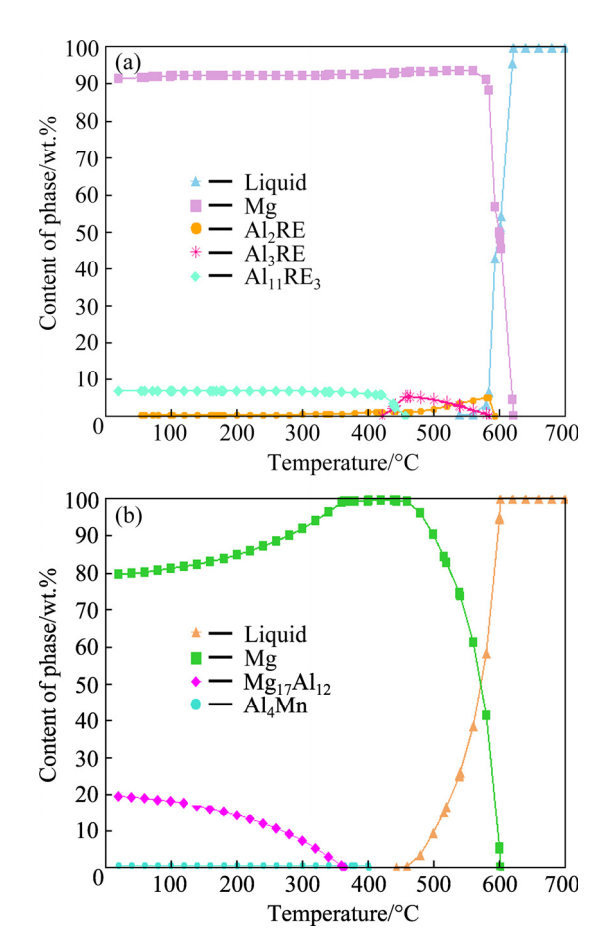


Fig. 9 Phase transformation process of AE44 (a) and AZ91D (b) alloys during equilibrium solidification process

Interestingly, this phenomenon also happens between Al₃RE and Al₁₁RE₃ phases. In addition, the solute rejection with the growth of α -Mg and the solute absorption with the growth of Al₁₁RE₃ lead to coupling growth of α -Mg and Al₁₁RE₃. Consequently, Al₁₁RE₃ is the dominant intermetallic phase in AE44 alloy with a lamellar-like morphology as mentioned above. And the particulate-shaped Al₂RE is scattered both within the α -Mg grains and among grain boundaries, while Al₃RE fails to be detected in the final microstructure of AE44 alloy. By comparing Fig. 9(a) with Fig. 9(b), it can be found that both the liquidus line and solidification curve of α -Mg in AE44 alloy are steeper than those of AZ91D alloy. In other words, the solidification temperature range of AE44 alloy is much narrower than that of AZ91D alloy. From classical solidification theory, a wider solidification temperature range will bring about a larger solidification contraction of the alloy, which is just the fundamental cause of porosities in the

form of shrinkage [36]. Meanwhile, coarse dendrites are prone to form with a wider solidification temperature range, making the feeding of the melt more difficult. In this case, shrinkage is formed in the remaining molten pools segmented by dendrite arms. Therefore, the narrower solidification temperature range of AE44 alloy is beneficial to reducing the formation of porosities in castings.

Another difference between the solidification characteristics of the two alloys involves with the release of latent heat during the precipitation of intermetallic phases. Since the dominant intermetallic phases in AE44 alloy are Al-RE serials phases and Mg-Al intermetallic phases fail to be detected, it can be concluded that the element Al preferentially reacts with RE rather than Mg. The formation of intermetallic phases is related to the mixing enthalpy between different elements. Taking the liquid phase as the reference state, the more negative the value of mixing enthalpy is, the more likely the corresponding intermetallic phases are formed accompanied with the release of a large amount of latent heat. In other words, the latent heat released during the precipitation of Al-RE intermetallic phases in AE44 alloy is larger than that of the precipitation of Mg-Al intermetallic phases in AZ91D alloy. This guarantees that the AE44 alloy has a better feeding capability during solidification, which is conducive to reducing the formation of porosities in the form of shrinkage in castings.

3.4 Formation mechanisms of defect bands

Based on the microstructure characterization on the cylindrical cross section of the middle tensile test bar, several important inferences can be drawn from the experimental results. According to the Scheil-Gulliver model of solidification [37,38], if the solidification front advances just in one-way from the casting surface to the center, the solute content in the solidified area should gradually increase due to the solute rejection with the continuous nucleation and growth of α -Mg in the melt. However, this is not the case in the HPDC AE44 alloy, as illustrated in Table 4. The solute content in the two defect bands is higher than that of the adjacent regions and the core region has the lowest solute content. Since the high content of solute in the defect bands exists mainly in the form

of Al₁₁RE₃ phase and the formation of this phase requires a relatively low temperature and high solute content in the remaining liquid, it can be determined that the area where defect bands are located is the final solidification area of castings. As for the core region, the lowest solute content can be attributed to the aggregation of a large number of ESCs, which also means that the melt in the core region has a relatively high solid fraction even in the early stage of solidification. In this case, the solidification front may advance not only from the casting surface to the center, but also from the casting center to the surrounding. Due to the contact with the cold die wall, a chilling surface layer with uniform and fine grains is formed rapidly in the melt, resulting in a relatively low solute content in the surface layer of castings. Though the solidification process of the melt in the die cavity is extremely complex, an inference can be drawn that the formation of the outer defect band is related to the chilling surface layer based on the fact that they are close to each other with a similar grain size and morphology. Meanwhile, the formation of the inner defect band is related to the core region which has an aggregation of a large number of ESCs.

To deeply understand formation mechanisms of defect bands, microstructure characterization was furtherly conducted on the longitudinal section of the middle tensile test bar with the purpose of studying the distribution of defect bands in the casting along the direction of melt flow. Moreover, since the formation of defect bands is generally considered to be related to the rheological and solidification behaviors of the alloy, the Anycasting software was used to analyze the filling and solidification process of the melt during the HPDC process in the present work. Figures 10 and 11 show the experimental and simulated results, respectively.

It can be seen from Fig. 10 that at the longitudinal section of the specimens, the defect bands also follow the outer contour of the casting. Both the inner and outer defect bands are clearly observed in the microstructure of the middle segment of the bar (Fig. 10(b)). However, at the transition segments both near and away from the ingate, only the outer defect band is observed, as illustrated in Figs. 10(a, c). The reason for this may be explained from the filling process of the melt. According to Figs. 11(a-d), the flowing melt is

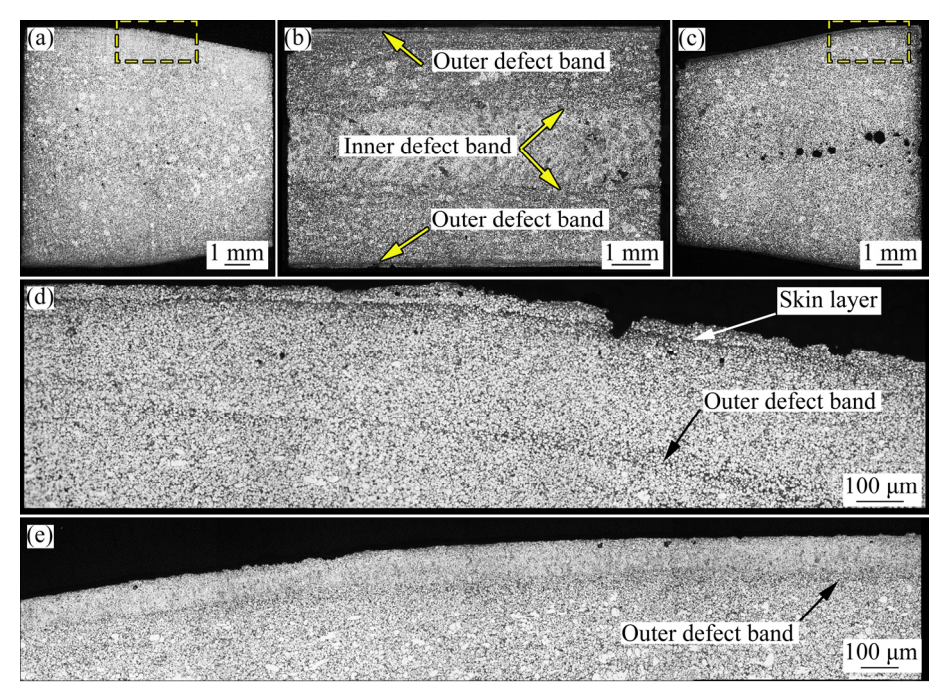


Fig. 10 OM images showing microstructure of different segments of longitudinal section: (a) Transition segment near ingate; (b) Middle segment; (c) Transition segment away from ingate; (d, e) Amplified views of rectangle regions marked in (a) and (c), respectively

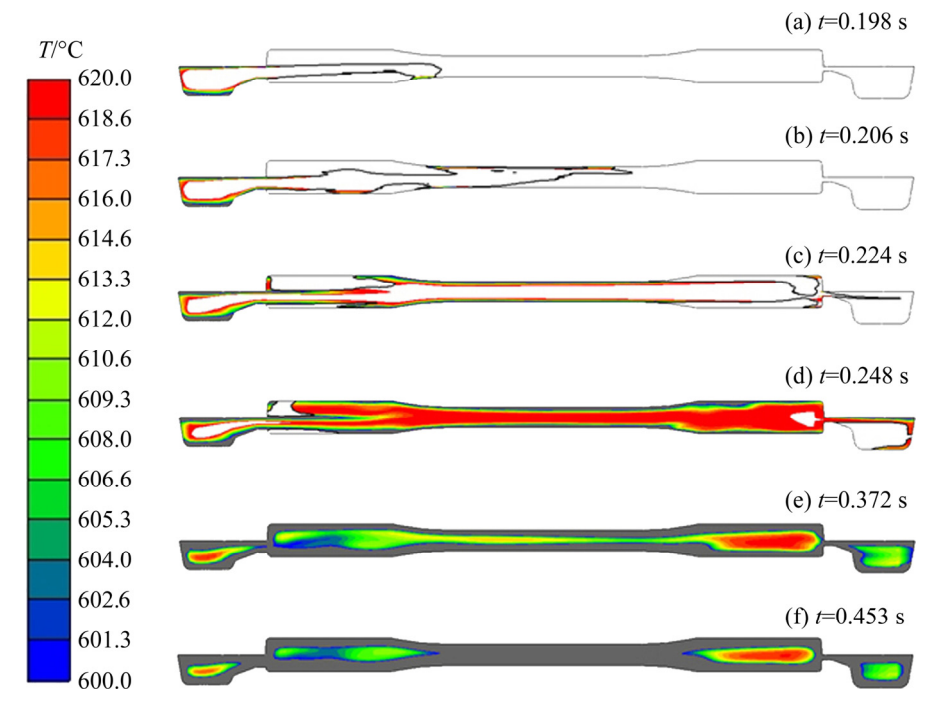


Fig. 11 Simulation of filling and solidification process of melt during HPDC process by Anycasting software

injected into the die cavity with a high speed through the ingate, leading to a remarkable difference in the flow patterns of the melt at different segments of the bar. The melt flow at the middle segment appears as a flow with relatively low Reynolds, while the flow state at the transition segments is extremely complicated. As previously proposed by LAUKLI et al [33], the floating ESCs migrate to the central region of the die cavity due to the force of the flowing melt, especially with a laminar-flow morphology. However, the ESCs are more dispersed with an irregular and turbulent flow

of the melt. This is just confirmed by the experimental results, as illustrated in Figs. 10(a-c), while the ESCs gather in the core region of the middle segment and are scattered in most areas of the longitudinal section of the transition segments. In other words, the formation of the inner defect band involves with the ESCs gathering in the core region of the casting. It can be seen from Figs. 11(c-e) that due to the contact with the cold die wall, the temperature of the melt decreases rapidly, resulting in formation of the chilling layer on the surface of the casting. Since the chilling layer is distributed on the whole casting surface, the outer defect band is commonly observed at different segments of the casting. It is noteworthy that the backflow of melt occurs at the transition segment near the ingate, as illustrated in Figs. 11(b-d). This can be just used to explain the formation of the skin layer on casting surface, as shown in Fig. 10(d), while more details on the skin layer can be found in Refs. [39,40]. Though the content of porosities in HPDC AE44 alloy is much less than that in HPDC AZ91D alloy as mentioned above, it can be seen from Fig. 11(f) that at the final solidification segment, a considerable number of porosities exist in the microstructure of the right end of the bar, as shown in Fig. 10(c).

In combination with the description of the rheological behavior of the partially solidified alloy made by DAHLE and JOHN [41], formation mechanisms of defect bands are proposed and enriched in present work, as illustrated in Fig. 12. As the filling and solidification proceed, there exists a solid fraction gradient of the melt in the die cavity. However, its direction is not simply from the casting surface to the center or vice versa due to the formation of the chilling layer and aggregation of the ESCs respectively on the surface and in the core region of the casting. Since the rheological behavior of the melt varies with different solid fractions, two critical solid fractions, f_c and f_p are defined for convenience of discussion. When the solid fraction is lower than the dendrite coherency point f_c , the melt behaves as a viscous fluid. At the solid fraction f_c , the grains gradually come into contact with each other, resulting in the formation of the grain network in the melt. The interaction among the grains produces shear strength to the network which is then capable of resisting a certain degree of deformation. According to the previously work conducted by DAHLE and JOHN [41], the value of f_c is strongly related to the grain morphology and size in the melt and it is typically in the range of 0.1–0.4. With the increase of solid fraction, the grain network in the melt can withstand a larger shear stress. When the solid fraction is higher than the maximum dendrite packing point f_p , the shear strength of the grain network increases rapidly. In this case, the grain network can undergo global deformation and exhibits more solid-like behavior. Similarly, with varied grain sizes and morphologies, different values of f_p can be expected while they are typically in the range of 0.3–0.7.

For the formation mechanism of the outer defect band, as illustrated in Fig. 12(a), there exists a semi-solid region next to the chilling surface layer. With the solid fraction of the surface layer close to 1, the solid fraction of the semi-solid region is in the range of f_c – f_p at some point even before the end of the filling process of the melt. Due to the shear stress induced by the melt flow just below the semi-solid region, the grain network formed in the semi-solid region is deformed gradually. Once the shear stress exceeds the shear strength limit of the grain network, it collapses associated with sliding and rotation of grains. Consequently, the semi-solid region expands, resulting in mass and interdendritic feeding to this region and then finally the formation of the outer defect band.

As for the formation mechanism of the inner defect band, it can be illustrated in Fig. 12(b) that in the core region, the solid fraction of the melt is likely to exceed f_p with the aggregation of a large number of coarse ESCs. Similarly, there exists a semi-solid region with the solid fraction in the range of f_c - f_p next to the core region. It is well known that at the last stage of the HPDC process, the intensification pressure is applied on the solidifying alloy, causing local shear stress in the semi-solid region. Likewise, collapse of the grain network happens when the shear stress reaches the shear strength limit of the grain network. With the expansion of the semi-solid region and feeding of the remaining melt to this region, a dilatant shear band is formed finally with positive macrosegregation. Here, the band is just the inner defect band discussed in the present work.

It is worth mentioning that the dendrite coherency can be achieved at a relatively low solid

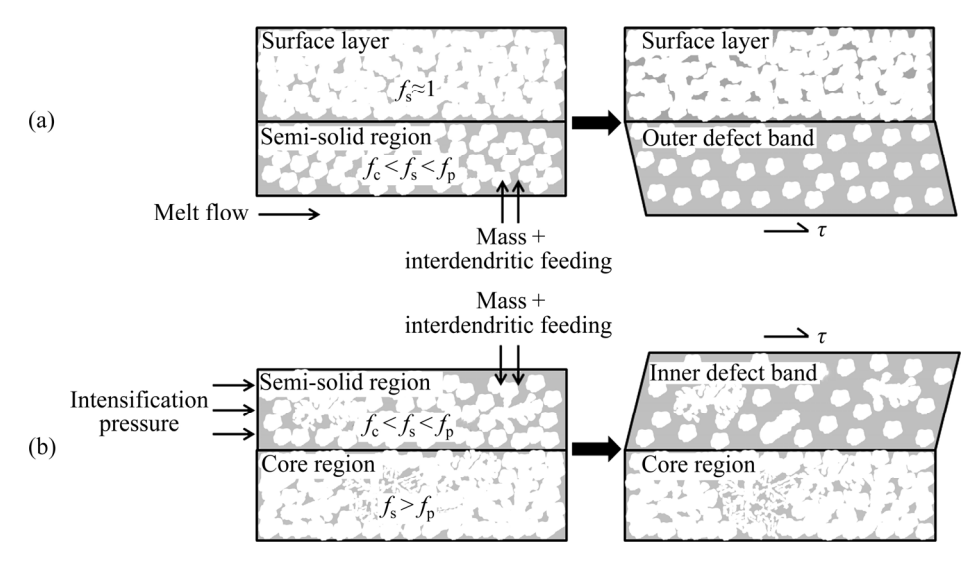


Fig. 12 Formation mechanisms of outer defect band (a) and inner defect band (b)

fraction of the melt with coarse dendritic grains, while it requires a higher solid fraction of the melt with smaller granular grains. Therefore, the value of f_c in the semi-solid region next to the surface layer is much larger than that in the semi-solid region next to the core region of the casting. A same conclusion can also be made on f_p . With a high cooling rate of the melt near the casting surface, its solid fraction gradient is much larger than that of the melt near the center. In this case, the width of the semi-solid region with the solid fraction just in the range of f_c - f_p next to the surface layer is narrower than that of the semi-solid region next to the core region. This just can be used to explain the reason why the inner defect band is much wider than the outer one.

4 Conclusions

- (1) Due to the appearance of double defect bands, the cylindrical cross section of die cast samples can be divided into five parts with different grain morphologies and size distributions.
- (2) The inner defect band is much wider than the outer one and both of them are solute segregation bands with a higher area fraction of Al₁₁RE₃ phase than that in the adjacent regions.
- (3) Unlike the defect bands in HPDC AZ91D alloy, no obvious aggregation of porosities is observed in the defect bands of AE44 alloy. This is due to a narrower solidification temperature range of AE44 alloy and a larger amount of latent heat released during the precipitation of intermetallic

phases. Both of them are beneficial to reducing the formation of porosities.

(4) The formation of the outer defect band is related to the chilling surface layer, while the formation of the inner defect band involves with the ESCs gathering in the core region of the casting. With the shear stress induced by the melt flow or intensification pressure acting upon the partially solidified alloy, the grain network collapses, resulting in the expansion of the semi-solid region and feeding of the remaining melt to this region and finally the formation of defect bands.

Acknowledgments

The authors are grateful for the financial supports from the the National Natural Science Foundation of China (No. 51805389), the Natural Science Foundation of Hubei Province, China (No. 2018CFB210), and the "111" Project, China (No. B17034)

References

- [1] SONG J F, SHE J, CHEN D L, PAN F S. Latest research advances on magnesium and magnesium alloys worldwide [J]. Journal of Magnesium and Alloys, 2020, 8: 1–41.
- [2] WANG X J, XU D K, WU R Z, CHEN X B, PENG Q M, JIN L, XIN Y C, ZHANG Z Q, LIU Y, CHEN X H, CHEN G, DENG K K, WANG H Y. What is going on in magnesium alloys? [J]. Journal of Materials Science & Technology, 2018, 34: 245–247.
- [3] JOOST W J, KRAJEWSKI P E. Towards magnesium alloys for high-volume automotive applications [J]. Scripta Materialia, 2017, 128: 107–112.

- [4] GUO K Y, XU C, LIN X P, YE J, ZHANG C, HUANG D. Microstructure and strengthening mechanism of Mg-5.88Zn-0.53Cu-0.16Zr alloy solidified under high pressure [J]. Transactions of Nonferrous Metals Society of China, 2020, 30(1): 99-109.
- [5] ZHANG W P, MA M L, YUAN J W, SHI G L, LI Y J, LI X G, ZHANG K. Microstructure and thermophysical properties of Mg-2Zn-xCu alloys [J]. Transactions of Nonferrous Metals Society of China, 2020, 30(7): 1803–1805.
- [6] WANG F, WANG Y, MAO P L, YU B Y, GUO Q Y. Effects of combined addition of Y and Ca on microstructure and mechanical properties of die casting AZ91 alloy [J]. Transactions of Nonferrous Metals Society of China, 2010, 20(S2): s311-s317.
- [7] WANG X J, ZHU S M, EASTON M A, GIBSON M A, SAVAGE G. Heat treatment of vacuum high pressure die cast magnesium alloy AZ91 [J]. International Journal of Cast Metals Research, 2014, 27(3): 161–166.
- [8] MERT F, ÖZDEMIR A, KAINER K U, HORT N. Influence of Ce addition on microstructure and mechanical properties of high pressure die cast AM50 magnesium alloy [J]. Transactions of Nonferrous Metals Society of China, 2013, 23(1): 66-72.
- [9] BAKKE P, PETTERSEN K, WESTENGEN H. Improving the strength and ductility of magnesium die-casting alloys via rare-earth addition [J]. JOM, 2003, 55: 46–51.
- [10] ZHU S M, NIE J F, GIBSON M A, EASTON M A, BAKKE P. Microstructure and creep behavior of high-pressure die-cast magnesium alloy AE44 [J]. Metallurgical and Materials Transactions A, 2012, 43: 4137–4144.
- [11] WANG Z Q, ZHANG B, LI D J, FRITZSCH R, ZHANG X Q, ROVEN H J, DING W J. Effect of heat treatment on microstructures and mechanical properties of high vacuum die casting Mg-8Gd-3Y-0.4Zr magnesium alloy [J]. Transactions of Nonferrous Metals Society of China, 2014, 24(12): 3762-3768.
- [12] DONG X X, FENG L Y, WANG S, NYBERG E A, JI S X. A new die-cast magnesium alloy for applications at higher elevated temperatures of 200–300 °C [J]. Journal of Magnesium and Alloys, 2021, 9: 90–101.
- [13] KUMAR D, PHANDEN R K, THAKUR L. A review on environment friendly and lightweight magnesium-based metal matrix composites and alloys [J]. Materials Today: Proceedings, 2021, 38: 359–364.
- [14] RZYCHOŃ T, KIEŁBUS A, ITYŃSKA-DOBRZYŃSKAL L. Microstructure, microstructural stability and mechanical properties of sand-cast Mg-4Al-4RE alloy [J]. Materials Characterization, 2013, 83: 21-34.
- [15] BI C, XIONG S M, LI X B, GUO Z P. Development of a fluid-particle model in simulating the motion of external solidified crystals and the evolution of defect bands in high-pressure die casting [J]. Metallurgical and Materials Transactions B, 2016, 47: 939–947.
- [16] ZHAO H D, BAI Y F, OUYANG X X, DONG P Y. Simulation of mold filling and prediction of gas entrapment on practical high pressure die castings [J]. Transactions of Nonferrous Metals Society of China, 2010, 20(11): 2064–2070.
- [17] ZHOU Y Q, GUO Z P, XIONG S M. Effect of runner design

- on the externally solidified crystals in vacuum die-cast Mg-3.0Nd-0.3Zn-0.6Zr alloy [J]. Journal of Materials Processing Technology, 2019, 267: 366-375.
- [18] LI X B, XIONG S M, GUO Z P. Correlation between porosity and fracture mechanism in high pressure die casting of AM60B alloy [J]. Journal of Materials Science & Technology, 2016, 32: 54–61.
- [19] LI X B, XIONG S M, GUO Z P. On the porosity induced by externally solidified crystals in high-pressure die-cast of AM60B alloy and its effect on crack initiation and propagation [J]. Materials Science and Engineering A, 2015, 633: 35–41.
- [20] WANG B S, XIONG S M. Effects of shot speed and biscuit thickness on externally solidified crystals of high-pressure diet cast AM60B magnesium alloy [J]. Transactions of Nonferrous Metals Society of China, 2011, 21(4): 767–772.
- [21] LI X B, XIONG S M, GUO Z P. Characterization of the grain structures in vacuum-assist high-pressure die casting AM60B alloy [J]. Acta Metallurgica Sinica-English Letters, 2016, 29(7): 619–628.
- [22] WANG Q L, XIONG S M. Vacuum assisted high-pressure die casting of AZ91D magnesium alloy at different slow shot speeds [J]. Transactions of Nonferrous Metals Society of China, 2014, 24(10): 3051–3059.
- [23] KANG H J, YOON P H, LEE G H, PARK J Y, JUNG B J, LEE J Y, LEE C U, KIM E S, CHOI Y S. Evaluation of the gas porosity and mechanical properties of vacuum assisted pore-free die-cast Al-Si-Cu alloy [J]. Vacuum, 2021, 184: 109917.
- [24] LI X B, XIONG S M, GUO Z P. Improved mechanical properties in vacuum-assist high-pressure die casting of AZ91D alloy [J]. Journal of Materials Processing Technology, 2016, 231: 1–7.
- [25] DAHLE AK, SANNES S, St. JOHN DH, WESTENGEN H. Formation of defect bands in high pressure die cast magnesium alloys [J]. Journal of Light Metals, 2001, 1: 99–103.
- [26] GOURLAY C M, MEYLAN B, DAHLE A K. Shear mechanisms at 0-50% solid during equiaxed dendritic solidification of an AZ91 magnesium alloy [J]. Acta Materialia, 2008, 56: 3403-3413.
- [27] GOURLAY C M, DAHLE A K. Dilatant shear bands in solidifying metals [J]. Nature, 2007, 445: 70-73.
- [28] CAO H, WESSEN M. Characteristics of microstructure and banded defects in die cast AM50 magnesium components [J]. International Journal of Cast Metals Research, 2005, 18: 377–384.
- [29] GOURLAY C M, LAUKLI H I, DAHLE A K. Defect band characteristics in Mg-Al and Al-Si high-pressure die castings [J]. Metallurgical and Materials Transactions A, 2007, 38: 1833–1844.
- [30] OTARAWANNA S, GOURLAY C M, LAUKLI H I, DAHLE A K. The thickness of defect bands in high-pressure die castings [J]. Materials Characterization, 2009, 60: 1432–1441.
- [31] LI X B, XIONG S M, GUO Z P. Influence of melt flow on the formation of defect band in high pressure die casting of AZ91D magnesium alloy [J]. Materials Characterization, 2017, 129: 344–352.

- [32] HUANG X S, HE L J, MI G B, LI P J. Characteristics of defect bands and their formation mechanisms in A356 wheel fabricated by horizontal squeeze casting [J]. Materials Science and Technology, 2015, 31: 400–408.
- [33] LAUKLI H I, GOURLAY C M, DAHLE A K. Migration of crystals during the filling of semi-solid castings [J]. Metallurgical and Materials Transactions A, 2005, 36: 805–818.
- [34] LI X B, XIONG S M, GUO Z P. On the tensile failure induced by defect band in high pressure die casting of AM60B magnesium alloy [J]. Materials Science and Engineering A, 2016, 674: 687–695.
- [35] YU W B, MA C S, MA Y H, XIONG S M. Correlation of 3D defect-band morphologies and mechanical properties in high pressure die casting magnesium alloy [J]. Journal of Materials Processing Technology, 2021, 288: 116853.
- [36] SU C Y, LI D J, WANG J, SHI R H, LUO Alan A, ZENG X Q, LIN Z H, CHEN J. Enhanced ductility in high-pressure

- die casting Mg-4Ce-xAl-0.5Mn alloys via modifying second phase [J]. Materials Science and Engineering A, 2020, 773: 138870.
- [37] SCHEIL E. Comments on the layer crystal formation [J]. Zeitschrift Fur Metallkunde, 1942, 34: 70–72.
- [38] GULLIVER G H. The quantitative effect of rapid cooling uopn the constitution of binary alloys [J]. Journal of the Institute of Metals, 1913, 9: 120–157.
- [39] YUAN Z H, GUO Z P, XIONG S M. Skin layer of A380 aluminium alloy die castings and its blistering during solution treatment [J]. Journal of Materials Science & Technology, 2019, 35(9): 1906–1916.
- [40] CHEN Z W. Skin solidification during high pressure die casting of Al-11Si-2Cu-1Fe alloy [J]. Materials Science and Engineering A, 2003, 348: 145-153.
- [41] DAHLE A K, ST. JOHN D H. Rheological behaviour of the mushy zone and its effect on the formation of casting defects during solidification [J]. Acta Materialia, 1999, 47: 31–41.

真空压铸镁合金 AE44 缺陷带的组织特征及形成机理

侯莹莹1, 吴孟武1, 田冰辉1, 李晓波2, 熊守美2

- 武汉理工大学 现代汽车零部件技术湖北省重点实验室,武汉 430070;
 清华大学 材料学院,北京 100084
- 摘 要:研究真空压铸镁合金 AE44 的显微组织,重点关注缺陷带的组织特征及形成机理。实验中普遍观察到的双缺陷带将压铸试样横截面划分为 5 个部分,各部分的晶粒形态与尺寸分布存在较大差异。心部缺陷带显著宽于表层缺陷带。双缺陷带均为溶质偏析带,AliiRE3 相面积分数均高于周围区域。压铸镁合金 AE44 缺陷带内未观察到明显的孔洞聚集现象,这是由镁合金 AE44 较窄的凝固温度区间以及金属间化合物相析出过程中释放出大量的潜热造成的。缺陷带的形成与作用于半固态合金的剪切应力有关,剪切应力会导致半固态区域晶粒骨架崩塌。然而,表层及心部缺陷带处的剪切应力形成机制大不相同。

关键词: 高压铸造; 镁合金; AE44; 显微组织; 缺陷带

(Edited by Bing YANG)